Simulation of a Mortar Launched, Parachute Deployed Battlefield Imaging System

Geoffrey Frost[1]
Mark Costello[2]

Department of Mechanical Engineering,
Oregon State University,
Corvallis, OR 97331

Flight behavior of a mortar launched, parachute deployed imaging system is examined with particular attention to characterizing the quantity and quality of recorded image data. Coverage area of the imager, blur due to motion of the imager, and view time are evaluated for different system configurations allowing important design parameters to be identified. It is shown that proper tailoring of the dynamic characteristics of the system greatly improves gathered image data quantity and quality. Coning of the canister is an important system characteristic that largely drives total ground coverage. Canister coning is influenced in a complex manner by system geometric parameters. Mounting the parachute riser to the canister in such a way that the connection is off the axis of symmetry of the canister is a powerful technique to increase coning of the canister. Likewise, increasing riser length also yields increased coning. Increasing spin rate of the canister leads to a proportional increase in image blur, which is largest toward the edge of the image. Also, increased canister weight tends to increase the descent rate, which reduces total view time. At the same time, increased descent rate increases the spin rate for cross type parachutes, leading to increased image blur. [DOI: 10.1115/1.1789974]

Introduction

This paper investigates dynamic modeling and performance of a mortar launched, parachute deployed imaging system that provides remote reconnaissance. This system will enable forward scouts to remain out of harms way while providing timely and critical information at the platoon level. The dynamic event considered consists of a cross type parachute borne sensor platform deployed from a mortar and the ensuing dynamics as it drifts to the ground. The cross-type parachute and sensor platform are contained within the nose of the mortar until deployment. Deployment occurs at a specified time by an explosive charge that separates the fore and aft sections of the mortar and ejects the sensor platform and its attached parachute out of the nose. The cross-type parachute inflates and decelerates the sensor platform. The sensor platform consists of a cylinder shaped canister fitted with a camera in its nose and the necessary electronics to transmit images back to a ground station. A schematic of the overall event is given in Fig. 1.

A number of models have been used to evaluate the dynamics of parachute and load systems in the atmosphere. White and Wolf [1] considered the stability of a parachute using a 5-degree-of-freedom model. They established that a large longitudinal disturbance on most parachutes results in large pitching motion, whereas a large lateral (out of the glide plane) disturbance causes large angle vertical coning motion. In a later study, Wolf [2] considered the stability of a parachute connected to a load using a 10-degree-of-freedom representation. Wolf established that stability is reduced as riser length is increased or parachute weight is increased. It was also noted that stability of a parachute is improved by increasing axial and normal aerodynamic force. Shpund and Levin [3] supported this notion in a parametric investigation they conducted on the aerodynamic characteristics of a group of cross-type parachutes. Their measurements showed an increase of up to 50% in the axial force due to spin, followed by a decrease in the longitudinal stability, leading to an increase in coning motion during descent. Doherr and Schilling [4] reported on the development of a 9-degree-of-freedom dynamic model to predict behavior of a parachute connected to a load. They found that rotating parachute systems are very sensitive to atmospheric disturbances and result in oscillations of the load with considerable amplitude. They also found that a dynamic model with more than 6-degrees-of-freedom are necessary with an appropriate mathematical model of the joint between the load and the parachute. This is in contrast to Neustadt, Ericksen, Guiteras, and Larrivee [5] who used a 6-degree-of-freedom mathematical analysis to study the dynamics of a payload-parachute system in which they concluded that computer results were in excellent agreement with test results. In a study conducted by Shpund and Levin [6], the effect of decreasing canopy to payload diameter ratio was experimentally investigated on cross-type rotating parachutes. The results showed a significant decrease in drag coefficient with decreasing diameter ratio. Similarly, an increase of the forebody's diameter yields a decrease in spin. Diameter ratio also affects static stability. This effect varies between improved stability for short cord configurations, commonly used for submunitions, to a reduction in stability when the cords are sufficiently longer. The investigation also included the effects of the canopy aspect ratio, different support systems, and the attachment diameter of the cords to the payload.

The use of image data and algorithms to identify and track objects is also fairly well developed. Algorithms have been applied to a host of different applications [7]. Example applications include missile guidance [8,9], autonomous navigation of highway vehicles [10–13], stellar tracking [14], ship motion [15], robot guidance [16–18], manufacturing [19], and solid modeling [20]. The usual procedure is to construct separate algorithms to identify where a particular target is within the field of view of the camera and subsequently rotate the camera within the field of regard so that the target object remains in the field of view of the camera for future recorded frames. Consideration of image distortion caused by camera and target dynamics during image recording is not normally considered. In the application of remote re-

[1]Graduate Research Assistant, Department of Mechanical Engineering, ORISE Fellow.

[2]Associate Professor, Department of Mechanical Engineering, Member ASME. The authors would like to thank Mr. Charles Hainz for his assistance in gathering the sample images presented in the paper.

Contributed by the Dynamic Systems, Measurement, and Control Division of THE AMERICAN SOCIETY OF MECHANICAL ENGINEERS for publication in the ASME JOURNAL OF DYNAMIC SYSTEMS, MEASUREMENT, AND CONTROL. Manuscript received by the ASME Dynamic Systems and Control Division November 6, 2003. Associate Editor: J. Tu.

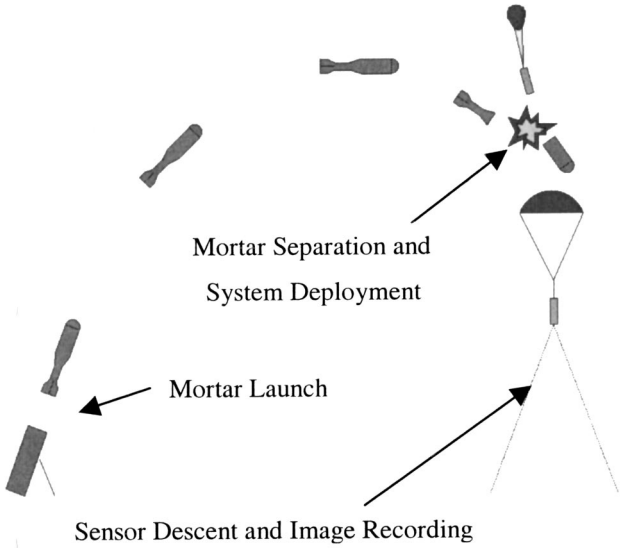

Fig. 1 Mortar launched, parachute deployed battlefield imaging system schematic

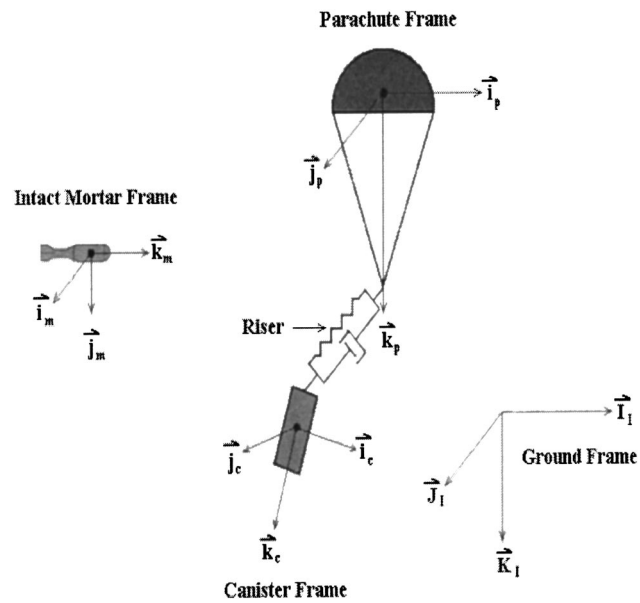

Fig. 2 Mortar and imaging system reference frames

connaissance at the platoon level it is necessary to obtain an image of the target that can be distinguished by a human forward observer [21–24].

Projectile and parachute-payload dynamics have not previously been integrated with optical system metrics in a simple manner to predict image quality based on simulated flight dynamics of a complete imaging system. Also, most previous efforts describing parachute-payload simulations do not consider deployment of the parachute-payload system. This paper simulates a parachute-payload imaging system that is deployed from a discharged mortar. A standard 6-degree-of-freedom model is used for the intact mortar. Once the mortar separates and the parachute payload system is deployed, a twelve degree-of-freedom model is used to predict the parachute-payload imaging system's trajectory, as well as six degrees-of-freedom to model the translational motion of the separated mortar round bodies. The work reported here develops formulas to estimate picture quality [25] using dynamic data recorded from a mortar launched, parachute deployed imaging system. The formulas are based on the state of the sensor platform at the time of imaging and individual camera parameters, such as, focal length, shutter speed, pixel size, and CCD size. The scale of an image, the amount of blur caused from motion of the camera, the ground area covered in each image and total ground area covered in a scenario are estimated to aid in the design of a real-time mortar launched imaging system. The influence of important system parameters, such as, canister to parachute attachment point, mass of the canister, center of gravity placement and camera specifications is documented.

Simulation Description

The intact mortar, the canister, and the parachute are modeled as rigid bodies with six degrees of freedom each. The degrees of freedom for each body include three position components of the mass center of the body as well as three Euler orientation angles of the body. A riser, modeled as a spring and damper, connects the canister and parachute. A diagram of the mortar and imaging system and the reference frames used to describe the systems is shown in Fig. 2. It is important to note that a nonconventional set of unit vector directions for the bodies is employed. In particular, the axis of symmetry for the bodies is the **k** unit vector, as opposed to the more conventional definition of **i**. The formation of the equations describing each rigid body is the same and the general formulas are given for a rigid body with six degrees of freedom. The subscript, B, is used to denote the body frame. The formulas for the intact mortar, the canister, and the parachute can be obtained by replacing the subscript, B, with the subscripts, M, C, and P, respectively.

The three translational degrees of freedom are the three components of the body mass center position vector,

$$\mathbf{r}_{O\to B}=x_B\mathbf{I}_I+y_B\mathbf{J}_I+z_B\mathbf{K}_I\,. \tag{1}$$

A sequence of rotations from the inertial frame to the body frame is defined by a set of body-fixed rotations that are ordered in the conventional manner. The three rotational degrees of freedom are the Euler roll angle (ϕ_B), pitch angle (θ_B), and yaw angle (ψ_B). The transformation from each body frame to the inertial frame is,

$$\begin{Bmatrix}\mathbf{I}_I\\ \mathbf{J}_I\\ \mathbf{K}_I\end{Bmatrix}=\begin{bmatrix} c_{\theta_B}c_{\psi_B} & s_{\phi_B}s_{\theta_B}c_{\psi_B}-c_{\phi_B}s_{\psi_B} & c_{\phi_B}s_{\theta_B}c_{\psi_B}+s_{\phi_B}s_{\psi_B}\\ c_{\theta_B}s_{\psi_B} & s_{\phi_B}s_{\theta_B}s_{\psi_B}+c_{\phi_B}c_{\psi_B} & c_{\phi_B}s_{\theta_B}s_{\psi_B}-s_{\phi_B}c_{\psi_B}\\ -s_{\theta_B} & s_{\phi_B}c_{\theta_B} & c_{\phi_B}c_{\theta_B}\end{bmatrix}\times\begin{Bmatrix}\mathbf{I}_B\\ \mathbf{J}_B\\ \mathbf{K}_B\end{Bmatrix}=[T_B]\begin{Bmatrix}\mathbf{I}_B\\ \mathbf{J}_B\\ \mathbf{K}_B\end{Bmatrix} \tag{2}$$

In the above equations and the equations shown below, the standard shorthand notation for trigonometric functions is used: $\sin(\alpha)\equiv s_\alpha$, $\cos(\alpha)\equiv c_\alpha$, $\tan(\alpha)\equiv t_\alpha$.

The mass center velocity vector of the body is defined in each of the reference frames discussed above,

$$\mathbf{V}_{B/I}=u_B\mathbf{I}_B+v_B\mathbf{J}_B+w_B\mathbf{K}_B=\dot{x}_B\mathbf{I}+\dot{y}_B\mathbf{J}_I+\dot{z}_B\mathbf{K}_I \tag{3}$$

as is the angular velocity vector of the body

$$\boldsymbol{\omega}_{B/I}=p\mathbf{I}_B+q\mathbf{J}_B+r\mathbf{K}_B\,. \tag{4}$$

Applying the transformation given in Eq. (2) to the mass center velocity components expressed in the body reference frame yields

$$\begin{Bmatrix}\dot{x}_B\\ \dot{y}_B\\ \dot{z}_B\end{Bmatrix}=[T_B]\begin{Bmatrix}u_B\\ v_B\\ w_B\end{Bmatrix} \tag{5}$$

Equating the projectile angular velocity vectors described using body frame components and using Euler angle rates generates

$$\begin{Bmatrix} \dot{\phi}_B \\ \dot{\theta}_B \\ \dot{\psi}_B \end{Bmatrix} = \begin{bmatrix} 1 & s_{\phi_B} t_{\theta_B} & c_{\phi_B} t_{\theta_B} \\ 0 & c_{\phi_B} & -s_{\phi_B} \\ 0 & s_{\phi_B}/c_{0_B} & c_{\phi_B}/c_{\theta_B} \end{bmatrix} \begin{Bmatrix} p_B \\ q_B \\ r_B \end{Bmatrix} \tag{6}$$

The kinetic differential equations are derived by considering the forces and moments associated with each individual body. Equation (7) gives the translational kinetic differential equation for each body,

$$m_B \mathbf{a}_{B/I} = \mathbf{F}_B \tag{7}$$

where,

$$\mathbf{a}_{B/I} = \frac{{}^B d\mathbf{V}_{B/I}}{dt} + \boldsymbol{\omega}_{B/I} \times \mathbf{V}_{B/I} \tag{8}$$

The rotational kinetic equation of motion for each body is given by

$$\frac{{}^I d\mathbf{H}_{B/I}}{dt} = \mathbf{M}_B \tag{9}$$

When expressed in component form the translational and rotational dynamic equations for each rigid body, including the intact mortar, the parachute, and the payload take the structure shown in Eqs. (10–11).

$$\begin{Bmatrix} \dot{u}_B \\ \dot{v}_B \\ \dot{w}_B \end{Bmatrix} = \begin{Bmatrix} X_B/m_B \\ Y_B/m_B \\ Z_B/m_B \end{Bmatrix} - \begin{bmatrix} 0 & -r_B & q_B \\ r & 0 & -p_B \\ -q_B & p_B & 0 \end{bmatrix} \begin{Bmatrix} u_B \\ v_B \\ w_B \end{Bmatrix} \tag{10}$$

$$\begin{Bmatrix} \dot{p}_B \\ \dot{q}_B \\ \dot{r}_B \end{Bmatrix} = [I_B]^{-1} \left[\begin{Bmatrix} L_B \\ M_B \\ N_B \end{Bmatrix} - \begin{bmatrix} 0 & -r_B & q_B \\ r_B & 0 & -p_B \\ -q_B & p_B & 0 \end{bmatrix} [I_B] \begin{Bmatrix} p_B \\ q_B \\ r_B \end{Bmatrix} \right] \tag{11}$$

During the initial phase of flight when the mortar round is intact, the mass, mass center location, and inertial properties of the mortar are based on the composite body. The intact mortar has applied load contributions from weight and body aerodynamic forces,

$$\begin{Bmatrix} X_M \\ Y_M \\ Z_M \end{Bmatrix} = \begin{Bmatrix} X_W \\ Y_W \\ Z_W \end{Bmatrix} + \begin{Bmatrix} X_A \\ Y_A \\ Z_A \end{Bmatrix} \tag{12}$$

while the canister and parachute both have applied load contributions from weight, body aerodynamic forces, separation forces and the riser connection force. Since the equations of motion are expressed in the body frame, all forces are expressed in the individual body frames.

$$\begin{Bmatrix} X_C \\ Y_C \\ Z_C \end{Bmatrix} = \begin{Bmatrix} X_P \\ Y_P \\ Z_P \end{Bmatrix} = \begin{Bmatrix} X_W \\ Y_W \\ Z_W \end{Bmatrix} + \begin{Bmatrix} X_A \\ Y_A \\ Z_A \end{Bmatrix} + \begin{Bmatrix} X_S \\ Y_S \\ Z_S \end{Bmatrix} + \begin{Bmatrix} X_R \\ Y_R \\ Z_R \end{Bmatrix} \tag{13}$$

For all bodies, the weight force takes on the following form

$$\begin{Bmatrix} X_W \\ Y_W \\ Z_W \end{Bmatrix} = W \begin{Bmatrix} -s_\theta \\ s_\phi c_\theta \\ c_\phi c_\theta \end{Bmatrix} \tag{14}$$

The aerodynamic force on the intact mortar uses a standard aerodynamic expansion

$$\begin{Bmatrix} X_A \\ Y_A \\ Z_A \end{Bmatrix} = \frac{1}{2} \rho V^2 D \begin{Bmatrix} C_{NA} \dfrac{u}{w} \\ C_{NA} \dfrac{v}{w} \\ C_{Z0} + C_{Z2} \dfrac{u^2+v^2}{w^2} \end{Bmatrix} \tag{15}$$

Prior to mortar separation the motions of the stowed canister and parachute are generated from kinematic relationships. After mortar separation, the fore and aft sections of the mortar are modeled as point masses with 3-degrees-of-freedom. The loads acting on the separated sections are weight, aerodynamic, and separation forces.

After the separation force has expired and the parachute has opened, the canister and parachute are modeled as rigid bodies, each with 6 degrees of freedom.

Equation (16) provides the aerodynamic force expression used for both the parachute and payload.

$$\begin{Bmatrix} X_A \\ Y_A \\ Z_A \end{Bmatrix} = -\frac{\pi}{2} \rho V^2 A \begin{Bmatrix} C_N u/V \\ C_N v/V \\ C_T \end{Bmatrix} \tag{16}$$

where

$$V = \sqrt{u^2+v^2+w^2} \tag{17}$$

The aerodynamic forces act at the center of pressure of the bodies. The aerodynamic coefficients for the parachute are obtained from standard wind tunnel tests and substituted directly into Eq. (16). The aerodynamic coefficients for the canister are obtained from published literature [4].

The above aerodynamic forces are not exerted on the canister until after the expulsion charge has elapsed [26,27]. Because of the complexity of canopy inflation, a simple quasi-static process based on the parachute's drag reference area is employed [28]. The mortar separates and the parachute deployment process begins after the expulsion charge has expired. Drag on the unopened parachute is substantially higher than the canister thus separating the two bodies. Canopy stretch occurs after the canister and parachute have separated a distance equal to the length of the cords plus the riser length. Drag area of the parachute is increased linearly for approximately 0.3 s during this phase. Full canopy inflation occurs at a much greater linear rate until the canopy has reached its full diameter. During canopy inflation the roll inducing moment of the parachute is assumed to be zero and the parachute has a spin rate equal to that of the canister. Once the parachute has reached its full diameter, Eq. (16) is used to generate the aerodynamic forces on the parachute.

To separate the mortar round and eject the parachute and canister, an equal and opposite force acting over a short time interval is exerted on the bodies. Equation (18) provides an expression for this force during separation.

$$\begin{Bmatrix} X_S \\ Y_S \\ Z_S \end{Bmatrix} = \pm P_S A \begin{Bmatrix} n_X \\ n_Y \\ n_Z \end{Bmatrix} \tag{18}$$

The pressure, P_S, from Eq. (18) is given as a 6th order polynomial when active and is equal to zero after the charge has expired. The forces are positive for the nose section of the round and negative for the parachute, canister and aft section of the round.

The riser force is caused by the elasticity of its material and is directed parallel to the riser line. The riser flexibility generates resistive stiffness and damping forces proportional to its extension and extension rate. Using the position and velocity of the riser attachment points, vectors describing the extension and extension rate can be formed.

$$\Delta L = \sqrt{(x_C - x_P)^2 + (y_C - y_P)^2 + (z_C - z_P)^2} \tag{19}$$

$$\Delta V = \frac{((x_C - x_P)(\dot{x}_C - \dot{x}_P) + (y_C - y_P)(\dot{y}_C - \dot{y}_P) + (z_C - z_P)(\dot{z}_C - \dot{z}_P))}{\Delta L} \tag{20}$$

Once Eq. (20) is formed, Eq. (21) is used to determine the magnitude of the riser force.

$$F_R = \begin{Bmatrix} k(\Delta L - L) + c\Delta V, & \Delta L - L \geqslant 0 \\ 0, & \Delta L - L \leqslant 0 \end{Bmatrix} \tag{21}$$

The second condition in Eq. (21) stipulates that when the riser is slack, no force is transmitted to the attachment points. The elastic riser force expressed in inertial coordinates is shown in Eq. (22).

$$\begin{Bmatrix} X_R \\ Y_R \\ Z_R \end{Bmatrix} = \frac{F_R}{\Delta L} \begin{Bmatrix} x_C - x_P \\ y_C - y_P \\ z_C - z_P \end{Bmatrix} \tag{22}$$

The total applied moments on the intact mortar contain contributions from steady body aerodynamics, and unsteady body aerodynamics

$$\begin{Bmatrix} L_M \\ M_M \\ N_M \end{Bmatrix} = \begin{Bmatrix} L_{SA} \\ M_{SA} \\ N_{SA} \end{Bmatrix} + \begin{Bmatrix} L_{UA} \\ M_{UA} \\ N_{UA} \end{Bmatrix} \tag{23}$$

while the total applied moments on the canister about its mass center contain contributions from the steady air loads, unsteady air loads, and the riser connection force.

$$\begin{Bmatrix} L_C \\ M_C \\ N_C \end{Bmatrix} = \begin{Bmatrix} L_{SA} \\ M_{SA} \\ N_{SA} \end{Bmatrix} + \begin{Bmatrix} L_{UA} \\ M_{UA} \\ N_{UA} \end{Bmatrix} + \begin{Bmatrix} L_R \\ M_R \\ N_R \end{Bmatrix} \tag{24}$$

The total applied moments on the parachute take on the same form as that of the canister. The mortar considered in this analysis is fin stabilized with a relatively low roll rate, so Magnus effects are not included in the aerodynamic expansion. The steady body aerodynamic moment is computed by a cross product between the distance vector from the center of gravity to the center of pressure and the steady body aerodynamic force vector above. The unsteady body aerodynamic moment provides a damping source for the angular motion of all the bodies and is given below.

$$\begin{Bmatrix} L_{UA} \\ M_{UA} \\ N_{UA} \end{Bmatrix} = \frac{1}{2}\rho V^2 D \begin{Bmatrix} \dfrac{pDC_{MQ}}{2V} \\ \dfrac{qDC_{MQ}}{2V} \\ C_{LDD} + \dfrac{rDC_{LP}}{2V} \end{Bmatrix} \tag{25}$$

For the parachute and payload, the moment due to the riser force is computed with a cross product between the distance vector from the mass center of the body to the location of the specific force. Note, for the parachute the center of pressure location and all aerodynamic coefficients depend on the angle of attack, while for the intact mortar the center of pressure and all aerodynamic coefficients depend on the Mach number of the mass center of the mortar. Mach number is computed at the center of gravity of the mortar. For the payload, the center of pressure is fixed at the geometric center. The aerodynamic angle of attack for the canister and parachute are calculated as shown in Eq. (26).

$$\alpha = \cos^{-1}\left(\frac{w}{V}\right) \tag{26}$$

Air density for the mortar, canister, and parachute is computed using the center of gravity position of the appropriate body in concert with the standard atmosphere [26]. Computationally, all aerodynamic coefficients and centers of pressure are obtained by a table look-up scheme using linear interpolation.

System Performance Metrics

Proper design of a real-time mortar launched parachute deployed imaging system requires that the canister mounted camera record images of a target area and be able to transmit those images to a ground station where they can be identified by a human observer. In order to evaluate image quality, the position and motion of the image plane of the camera must be known in the ground reference frame (see Fig. 3). The position of the image plane and the camera focal point with respect to the canister reference frame located on the canister's center of gravity is known from the basic camera configuration. The center of gravity of the canister in the inertial ground frame is known from the flight dynamic model described above. The position in the ground reference frame of a point on the image plane and the focal point of the camera is calculated using the following kinematic relationship.

$$\begin{Bmatrix} x_i \\ y_i \\ z_i \end{Bmatrix} = \begin{Bmatrix} x_c \\ y_c \\ z_c \end{Bmatrix} + \begin{bmatrix} c_\theta c_\psi & s_\phi s_\theta c_\psi - c_\phi s_\psi & c_\phi s_\theta c_\psi + s_\phi s_\psi \\ c_\theta s_\psi & s_\phi s_\theta s_\psi + c_\phi c_\psi & c_\phi s_\theta s_\psi - s_\phi c_\psi \\ -s_\theta & s_\phi c_\theta & c_\phi c_\theta \end{bmatrix}_c \begin{Bmatrix} r_x \\ r_y \\ r_z \end{Bmatrix}_i \tag{27}$$

With the focal point and the point of interest on the image plane known in the ground reference frame, the projection of the point in the ground plane is determined using similar triangles in Eq. (28) (see Fig. 3). The variable, z_g, is the height of the ground surface above sea level and is assumed to be 10 m.

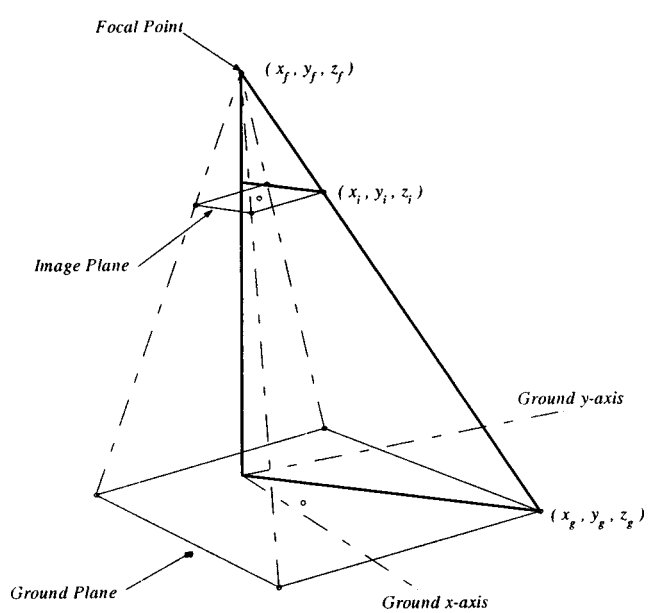

Fig. 3 System metrics

$$\begin{Bmatrix} x_g \\ y_g \\ z_g \end{Bmatrix} = \begin{Bmatrix} x_f + \dfrac{(z_g - z_f)(x_i - x_f)}{(z_i - z_f)} \\ y_f + \dfrac{(z_g - z_f)(y_i - y_f)}{(z_i - z_f)} \\ z_g \end{Bmatrix} \tag{28}$$

A polygon representing the image captured by the camera is obtained by projecting the four corners of the image plane onto the ground plane. Thus, the amount of ground area captured by each image is determined by calculating the area of the projected polygon. Total area of coverage for an individual scenario is determined by using an algorithm that sums the ground area captured by each image and subtracts areas of image overlap.

A determining factor in image clarity is resolution. The camera must be within a prescribed distance of the ground so that target effects are visible on the recorded images. As the camera nears the ground, the ground area in view decreases and the picture clarity increases, therefore the rate of descent is important to determine how many useful images can be transmitted at the appropriate distance from the ground with an acceptable resolution. The resolution, or amount of detail in a frame, is a function of the size of pixels, the focal length of the imager, and the distance from the ground plane to the image plane. Pixel sizes and focal lengths vary for different cameras. The size of the area mapped to an individual pixel, or pixel scale, is determined using Eq. (29).

$$P_X = \frac{P_L(z_g - z_f)}{(z_i - z_f)} \tag{29}$$

Buildings and roads can be distinguished in an image of an urban setting where the area captured by each pixel measures 2×2 m on the ground. Vehicles can be recognized in an image captured at an altitude where each pixel measures 0.5×0.5 m on the ground. More details on image resolution can be found in Ref. [29].

Another factor concerning picture clarity is image smearing. Images from cameras with high exposure rates can become smeared, or blurred, if the canister's roll rate is too high or its lateral oscillations are too drastic. Therefore, the canister roll rate and lateral oscillations must be limited to avoid image smearing for cameras with high exposure times. Pixel blur is defined as the number of pixels a point in the ground plane moves through in a single exposure time. Pixel blur is determined by multiplying the velocity of the projection of a point in the ground plane by the exposure time, or shutter speed of the camera, and dividing by the pixel scale. Differentiating Eq. (28), and determining the magnitude yields the velocity of a projected point in the ground plane shown in Eq. (30).

$$V_g = \sqrt{\dot{x}_g^2 + \dot{y}_g^2} \tag{30}$$

The pixel blur function is shown in Eq. (31).

$$P_B = \frac{V_g t_{ss}}{P_X} \tag{31}$$

Figures 4–6 show a series of images taken with increasing amounts of pixel blur. The images were taken with a Sony—Mavica MVCFD91 digital camera from a moving car 3.048 m away from the display panel. The accuracy of the speedometer was estimated at ±4.0 kph. To achieve the designated amounts of pixel blur at reasonable driving speeds, it was necessary to take the images at varying shutter speeds. As a result the images have different pixel blur tolerances. The camera has a resolution of 1024×768 pixels with a pixel size of 6.5 μm and was set at a focal length of 5.2 mm. From Eq. (29), pixel scale was determined to be 3.84 mm/pixel. By comparing the moving images to the almost still image in Fig. 4 an idea of the level of detail that can be visually discerned at a certain amount of pixel blur can be realized. For pixel blur of less than 10 pixels all the objects present can be determined and a great amount of detail can be observed. At a range of 10–30 pixels of blur the objects present such as the tank and the beaver head are still readily detectable, but the detail such as the words and shape of the turret become much less discernible. Beyond 30 pixels of blur, objects begin to become imperceptible. Without trying to make a statement about perception abilities of analysts it is doubtful that if the image in Fig. 4 had not been viewed first that any of the objects in Fig. 6 could be recognized.

Fig. 4 Moving image, pixel blur=2.0±0.5 pixels

Fig. 5 Moving image, pixel blur=10.0±3.0 pixels

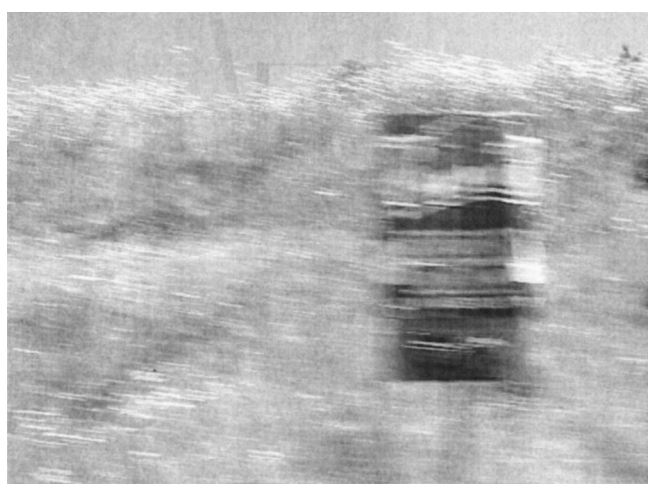

Fig. 6 Moving image, pixel blur=40±5.0 pixels

Table 1 – Nominal System Data					
	Symbol	Units	Parachute	Canister	Mortar
Weight	W	N	1.646	6.896	116.988
Vector from 0 to center of gravity	r_x	m	0.000	0.000	0.000
(Body-Fixed)	r_y	m	0.000	0.000	0.000
	r_z	m	0.751	0.085	variable
Reference Diameter	D	m	1.054	0.070	0.120
Length	L	m	2.097	0.131	
Riser Length	l	m	0.152	N/A	N/A
Vector from 0 to riser	r_x	m	0.000	0.000	N/A
(Body-Fixed)	r_y	m	0.000	0.000	N/A
	r_z	m	2.097	-0.011	N/A
Centroidal Inertial Properties	I_{XX}	kg-m^2	157E-3	5.65E-3	8.24
	I_{YY}	kg-m^2	157E-3	5.65E-3	8.24
	I_{ZZ}	kg-m^2	3.40E-3	0.47E-3	0.78
Vector from 0 to Center of	r_x	m	0.000	0.000	0.000
Pressure (Body-Fixed)	r_y	m	0.000	0.000	0.000
	r_z	m	0.277	0.087	Mach Dependent
Tangential Force Coefficient	C_T		AOA Dependent	AOA Dependent	Mach Dependent
Normal Force Coefficient	C_N		AOA Dependent	AOA Dependent	Mach Dependent
Rolling Moment Coefficient	C_{DD}		AOA Dependent	0.000	Mach Dependent
Pitch Damping Coefficient	C_{MQ}		AOA Dependent	-20.000	Mach Dependent
Roll Damping Coefficient	C_{LP}		AOA Dependent	0.000	Mach Dependent
Bearing Joint Damping Coefficient	C_B / I	N m s/rad	0.050	0.0503	N/A
Fixed Joint Damping Coefficient	C_F / I	N m s/rad	0.111	0.111	N/A
Fixed Joint Stiffness Coefficient		N m/rad	14.796	14.796	N/A

Nominal System Response

The equations of motion described above are numerically integrated using a fourth order Runge–Kutta algorithm to generate the trajectory of the intact mortar round and the parachute and canister after deployment. Simulation of a nominal system under different conditions is performed to demonstrate the dynamic performance and image quality of the system. Nominal system data is recorded in Table 1. Aerodynamic coefficient data for the intact mortar was predicted using the projectile design and analysis computer code, PRODAS [8]. The parachute is a cross-type and its aerodynamic coefficient data was obtained from a study conducted by Shpund and Levin [3]. The canister's aerodynamic coefficient data was obtained from Doherr and Schilling [4]. The initial results considered are representative of a nominal simulation with no atmospheric winds. Figures 7–9 show the altitude, velocity, and roll-rate time histories for all the components of the mortar launched, parachute deployed battlefield imaging system. The sequence of events is discussed in separate sections and the above figures should be referred to where appropriate.

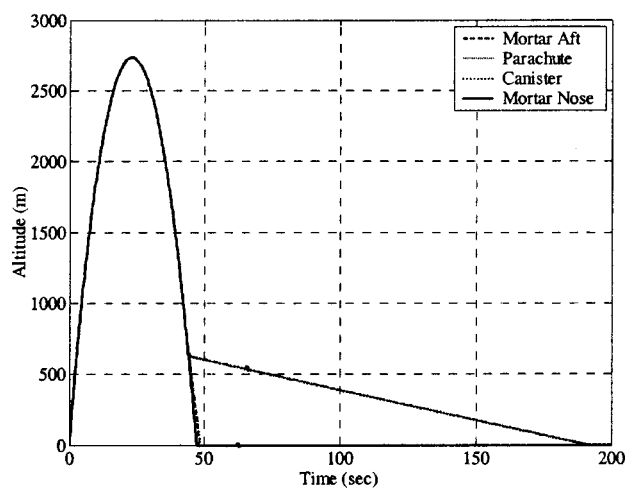

Fig. 7 Altitude time history (nominal)

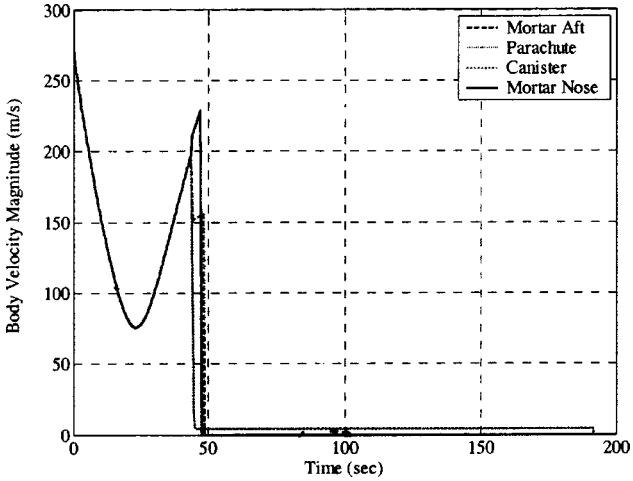

Fig. 8 Body velocity time history (nominal)

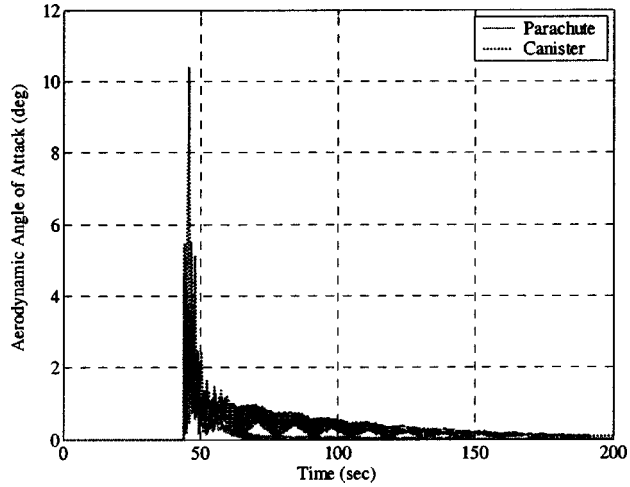

Fig. 10 Canister and parachute angle of attack time history (nominal)

Nominal Scenario. In the nominal scenario, the mortar exits the muzzle with a velocity of 261 m/s at a pitch angle of 70 deg from horizontal. The mortar separates and the parachute and canister are deployed 43.75 s into the flight. The camera is activated 50 s into flight. The trajectories of the various components coincide during the intact mortar flight phase. The trajectories diverge at the point of mortar separation.

Mortar Flight. The intact mortar orientation is stable and typical for this type of round. The intact mortar leaves the muzzle at its initial velocity and slows to a velocity of roughly 76 m/s as it reaches its apex approximately 23 s into its flight. The mortar pitches over and accelerates towards its steady state drop velocity. It continues to pitch down to an angle of approximately −70 deg from horizontal and travels downrange approximately 3380 m at which point the mortar separates and the imaging system is expelled. The mortar has slight fin cant, generating roll, and causing the system to deviate approximately 35 m laterally. After separation the nose and aft components continue to travel down range until they impact the ground.

Separation. At 43.75 s the expulsion charge is detonated and the force, acting in equal and opposite directions, accelerates the nose of the mortar and decelerates the aft mortar section, parachute, and canister. The nose and the aft mortar section accelerate toward their steady state drop velocities and the parachute opens and further decelerates the canister. The parachute initially separates from the canister a distance equal to the length of the cords plus the riser length. When it reaches this distance the parachute opens and the sudden increase in drag stretches the riser. This stretch results in a 913 N load in the riser. Once this initial shock damps, the force in the riser becomes steady at a load equal to the weight of the canister, approximately 6.8 N. The drag of the parachute slows the forward motion of the canister and they both descend almost vertically at a range of approximately 3390 m. The lateral motion of the canister and parachute is quickly diminished by parachute drag.

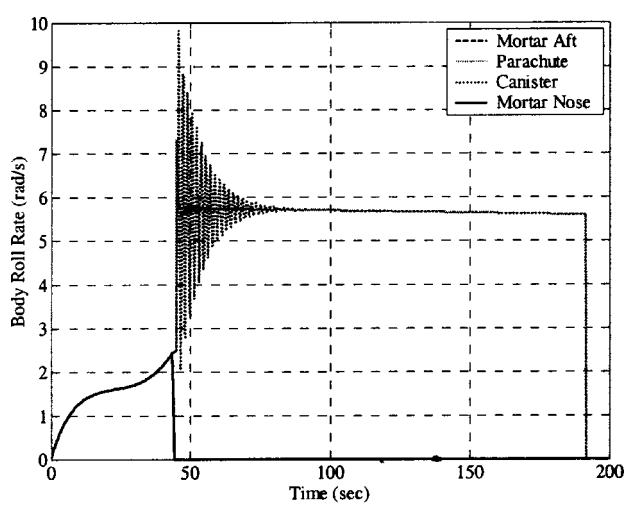

Fig. 9 Roll rate time history (nominal)

Parachute and Canister Flight. Cross-type parachutes are designed to rotate to increase vertical axial force. This rotation decreases longitudinal stability, which explains the tendency of this type of parachute to experience coning motion during descent [3]. This coning motion is responsible for the notable oscillations after inflation that gradually lessen as the system reaches steady state. The nominal system incorporates a fixed joint to attach the canister to the parachute riser, thus the parachute cords act as a rotational spring and damper. As the parachute generates roll, the cords twist causing the canister to spin. The parachute and canister system's drop velocity stabilizes at approximately 4.3 m/s. However, there is a very slight decrease in the descent rate. This is due to the parachute's slightly increasing roll rate, which increases vertical axial force. It can be seen in Fig. 9 that the spin of the mortar is imparted to the canister and the parachute at the time of separation. The spin rate of a cross-type parachute is proportional to the square of the forward velocity. The initial velocity of the parachute as it exits the round is such that it causes the parachute to promptly spin up once it opens. However, due to the high drag of the parachute, its velocity decreases rapidly, and consequently its roll rate damps quickly. Due to cord twist canister roll rate increases as the parachute spins up and oscillates about the rate of the parachute until it damps around 110 s. Angles of attack of the parachute and canister shown in Fig. 10 exhibit coning motion mentioned earlier. Angle of attack of the canister is greater than that of the parachute because coning motion of the parachute is amplified by the lever action of the parachute cord length.

Camera Performance. After the camera is turned on at an altitude of 600 m, it remains aloft and is consequently able to record images for approximately 141 s (Fig. 7). The imaging rate used for this simulation is 15 frames/s. Therefore, the imager is able to record approximately 2115 images before it impacts the ground. Note that imaging rate should not be confused with exposure time. Imaging rate takes into account transmission time of

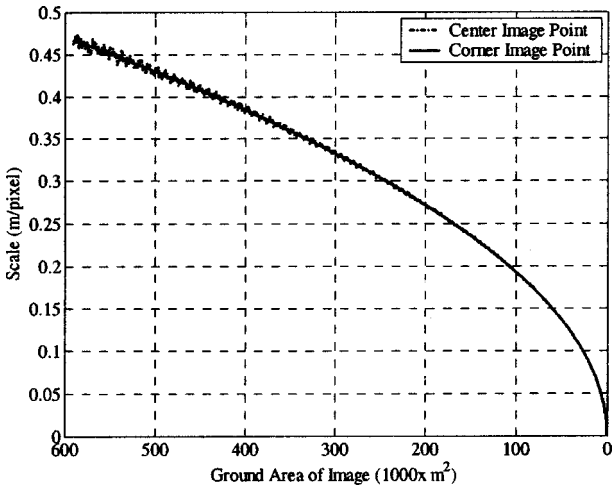

Fig. 11 Pixel scale (resolution) versus ground area captured (nominal)

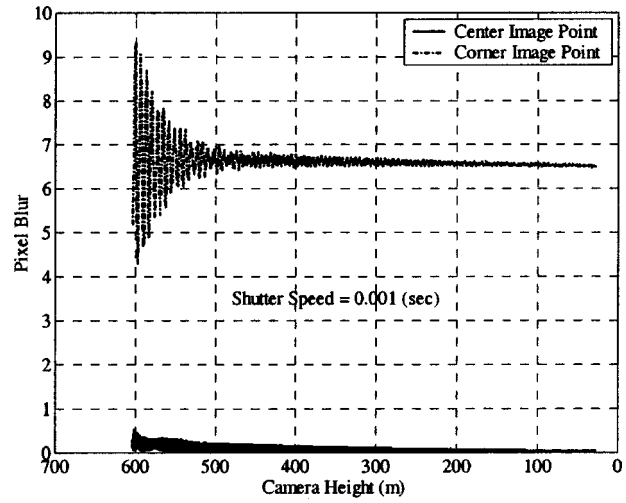

Fig. 12 Pixel blur (clarity) versus camera height (nominal)

the captured image, and recording time as well. Cameras with higher resolutions, or more pixels per CCD may improve the quality of an image, but they also result in more data that must be recorded and transmitted, thus resulting in lower imaging rates.

In the following figures demonstrating image quality of a system, data is reported for an image point located at the center of the image plane and an image point at one corner of the image plane. These points were chosen to exhibit the difference in image quality between the center and the edges of the image. Because the motion of the canister is such that all corner points exhibit similar trends it is only necessary to report a single corner point to demonstrate edge image quality. During a nominal flight the imager is able to capture a total of 919,000 m^2 of ground area. However, the resolution at which the area is captured varies over the duration of the flight. Figure 11 shows pixel scale versus the amount of ground area in each image for an image point located at the center of the image plane and an image point located at the corner of the image plane. For example, the first image captured in the nominal scenario records an area of approximately 590,000 m^2 with a resolution of 0.46 m/pixel. At this resolution objects such as a car would be discernible. Resolution improves linearly as the camera nears the ground, however a smaller amount of area is captured in each image. Note that approximately 65% of the total ground area captured during the flight is gained in the first image, indicating that of the 2115 images taken, there is a great amount of overlap. Before an image can be considered discernible by an analyst, the clarity of the image must be evaluated. Figure 12 shows pixel blur for a shutter speed of 1 ms versus camera height for the nominal system scenario. Because the camera is spinning the motion of the edge points is greater than those at the center resulting in more pixel blur. It can be seen in Fig. 12 that rotational vibration of the camera due to cord twist shown in Fig. 9 results in large fluctuations of pixel blur at the edges of the image, however it has little effect at center of the image. The smaller oscillations in pixel blur after rotational vibration due to cord twist is damped are a result of the coning motion of the system further referred to as canister oscillation. Pixel blur is linearly proportional to shutter speed and therefore varying shutter speed changes pixel blur by a proportional amount. For example, if the same scenario was conducted with a 10 ms shutter speed the amount of pixel blur would be 10 times greater and consequently the image would be much less discernible.

Joint Type. For this simulation all system parameters were held at nominal values except for the type of joint used to attach the parachute riser to the canister. Instead of a fixed joint, a radial bearing type joint was used. Similar trends were observed for all time traces except for roll rate of system components. A radial bearing joint does not allow the cords to twist as the parachute spins up, therefore the only moment that acts on the canister from the parachute rotational motion is due to friction in the bearing. In Fig. 13 it can be seen that roll rate of the canister gradually increases until it reaches that of the parachute. Thus, the bearing joint eliminates erratic canister motion present immediately after parachute inflation for a system with a fixed joint (see Fig. 9). As a result less blur is present at higher camera altitudes with lower resolutions (Fig. 14).

Parametric Trends

The effect of canister weight, canister mass center location, riser length, and riser attachment offset are considered against the image system metrics defined earlier. These trends are compared in Figs. 15–21.

Effect of Canister Weight. The average rate of descent after the camera has been activated and the number of images captured versus a range of canister weights is shown in Fig. 15. As the weight of the canister is increased the average rate of descent increases and consequently the number of images able to be captured decreases. Also, as the rate of descent or axial velocity of the parachute increases so does its spin rate, thus increasing the spin

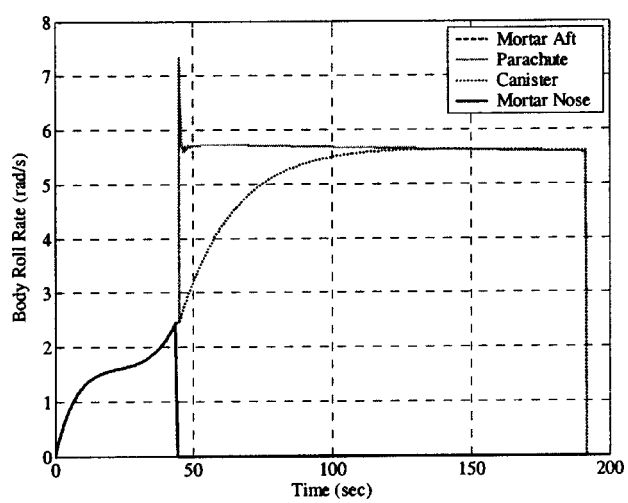

Fig. 13 Roll rate time history (nominal—bearing joint)

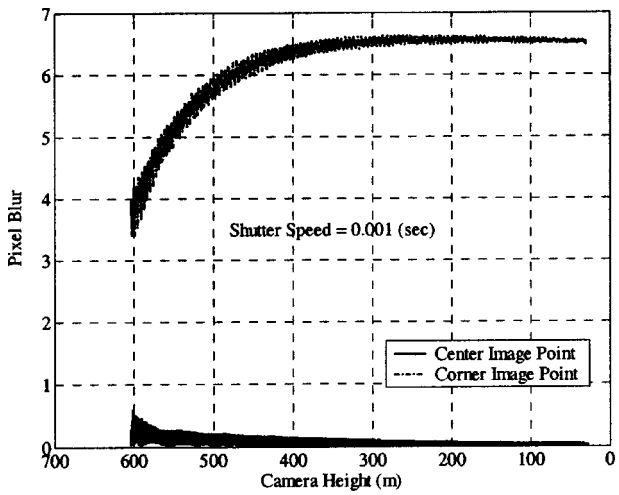

Fig. 14 Pixel blur (clarity) versus camera height (nominal—bearing joint)

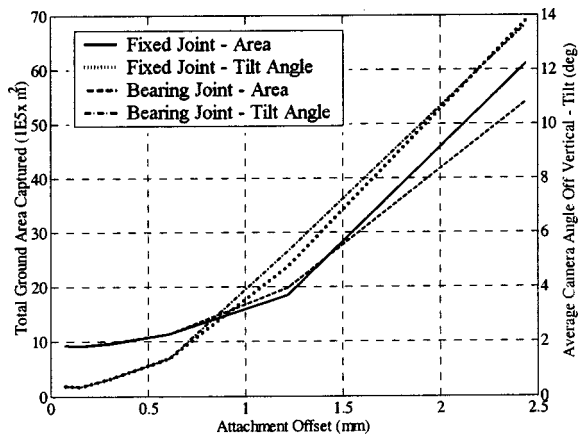

Fig. 16 Total ground area and average camera angle off vertical versus riser length

rate of the canister. A direct result of this increased spin rate is an increase in the amount of pixel blur near the edges of the images captured. Average pixel blur at the edges of the image for a nominal system is approximately 6.6. Increasing the weight of the canister to 71.17 N increases the average pixel blur for a fixed joint system to approximately 19. Initially after parachute inflation, however, fixed joint systems exhibit an oscillatory flight behavior that results in pixel blur per canister oscillation varying up to a range that is approximately 50% of the average. Oscillatory canister motion for a fixed joint system immediately after parachute inflation is not present for a bearing joint system and the amount of blur is less at higher altitudes and lower resolutions. For a bearing joint system pixel blur for a 71.17 N canister is initially around 4 and increases to approximately 16 at which point the canister contacts the ground. The range of pixel blur per canister oscillation remains fairly constant for a bearing joint system and is less than 2% of the average. The pixel blur for the center image points as stated before is not greatly affected by the spin rate of the canister and the pixel blur for these points for the individual canister weights more or less are the same for the range of canister weights. As stated before, the pixel scale as a function of camera height is not significantly affected by the weight of the canister or the type of joint used. Heavier canisters result in increased spin rates, but decrease the coning motion of the parachute and thus the projected image does not sweep out as large of an area on the ground. Note that most of the total ground area captured is in the first few images, and for the fixed joint system these images are of the poorest quality because of the excessive blur and low resolution. However, for a bearing joint system the amount of blur evident in these first images is less than those captured by a fixed joint system and, consequently, a greater amount of identifiable ground area coverage is gained.

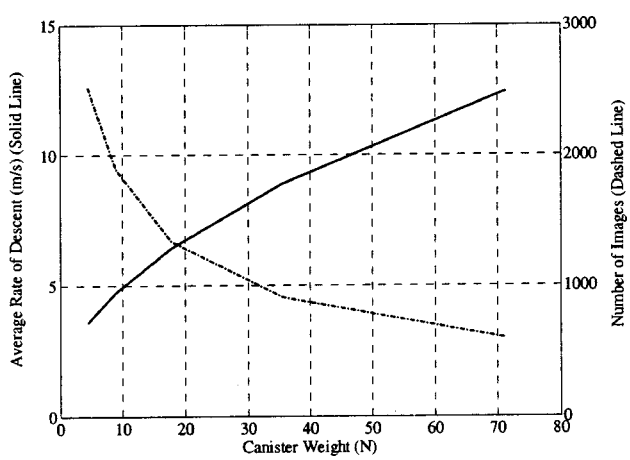

Fig. 15 Average rate of descent and number of images captured versus canister weight

Effect of Riser Length. Figure 16 shows the total ground area captured and the average camera tilt after steady state has been reached versus riser length. Pixel blur at the edge of the image is significantly greater than that of the center of the image. This is the case for all the studies conducted and therefore the trends for the center of the image are not discussed in the following studies. Because wind is not considered and the system descends vertically the angle of attack and the camera angle off vertical or tilt as referred to by aerial photographers can be considered identical. Increasing riser length effectively increases camera tilt and thus sweeps out larger ground area. A side effect though is that pixel blur vibrates through a greater range as the canister oscillates. This effect is shown in Fig. 17, where the average edge pixel blur after steady state along with the range of pixel blur per canister oscillation is shown versus riser length. The increased riser length amplifies the moment produced about the canister center of gravity due to the coning motion of the parachute and thus increases canister oscillations. It is apparent from Figs. 16 and 17 that the type of joint used does not significantly effect image performance of the system for increased riser length.

Effect of Canister Mass Center Location. In Figs. 18 and 19, the mass center of the canister was placed forward of the nominal position in 9.14 mm increments up to 45.72 mm. This can be viewed as moving the center of gravity towards the ground if the canister were hanging vertically beneath the parachute. Moving the canister center of gravity forward exhibits a similar trend of increased pixel blur range per canister oscillation like increasing the riser length. In this case, this is due to the fact that the moment arm from the canister center of gravity to the attachment point is increased. Therefore, the moment about the canister center of gravity due to the force in the riser caused by the coning motion of the parachute is amplified causing larger oscillations of the canister. Figure 18 shows total ground area captured and average camera tilt versus location of the canister mass center. Joint type has little effect on tilt angle variation with change in CG location and the two curves appear to lie on top of each other. Figure 19 shows average edge pixel blur after steady state and pixel blur range per canister oscillation versus change in forward location of the canister mass center.

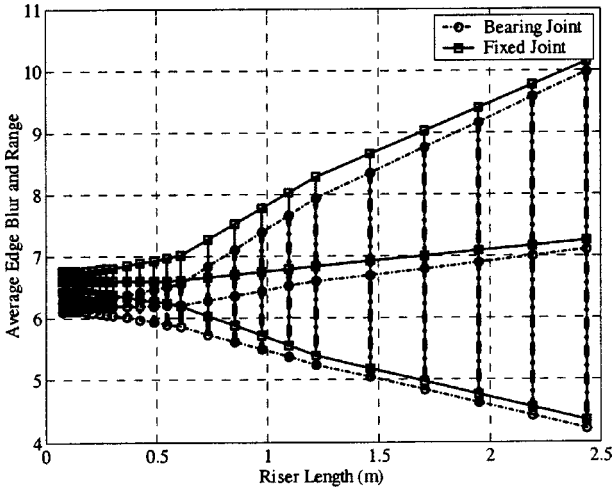

Fig. 17 Average pixel blur and range of pixel blur per canister oscillation versus riser length

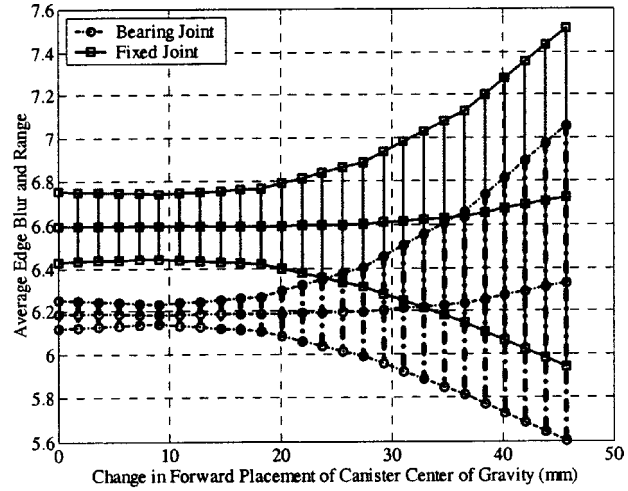

Fig. 19 Average edge pixel blur and range of pixel blur per canister oscillation versus change in forward placement of the canister center of gravity

Effect of Riser Attachment Offset. Canister offset is defined as mounting the parachute riser to the canister in such a way that the connection is off the axis of symmetry of the canister. For both the bearing joint and the fixed joint systems, pixel blur behavior is very erratic until canister spin rate stabilizes at the same rate of the parachute. The range of pixel blur per canister oscillation also tends to decay in the course of the flight. The point at which this occurs is considered the steady state of the system for this study. Images captured after steady state are higher resolution, however for a bearing joint, an offset attachment produces more erratic behavior than for a center-attached system. Also, an offset fixed joint produces greater deviations in pixel blur immediately after parachute inflation than a nominal system. Thus, images recorded shortly after parachute inflation are not reliable estimates of the ground area captured and image quality is reported for the system after it has stabilized. This is considered to have occurred at approximately a height of 500 m. Figure 20 shows total ground area covered and camera angle off vertical for a range of riser attachment offsets. Camera tilt is greater for a fixed joint system and consequently a greater sweep of ground area is captured during its descent than a bearing joint system. Both offset systems capture much greater ground area than a center-attached system due to the sweeping motion of the canister as it rotates. However, as shown in Fig. 21 an offset bearing joint produces less average pixel blur at a corner point after steady state is achieved.

Conclusions

Simulation of a mortar launched, parachute deployed, imaging system that integrates dynamic behavior with imaging performance has been developed and employed to predict image quantity and quality for an exemplar mortar launched, parachute deployed, imaging system. Through proper tailoring of dynamic characteristics of the payload and parachute configuration, image performance can be greatly enhanced. In particular, increased canister weight increases the descent rate of the system, which consequently increases the spin rate for cross type parachutes. This leads to a proportional increase in image blur, which is largest toward the edge of the image. Also, coning of the canister in general increases total ground coverage area while causing image blur to increase only slightly. Locating the attachment point of the parachute riser to the canister off the axis of symmetry is an effective technique to increase coning. However, offsetting the attachment point causes large initial oscillations after deployment from the mortar, which yields unreliable images. Increasing riser

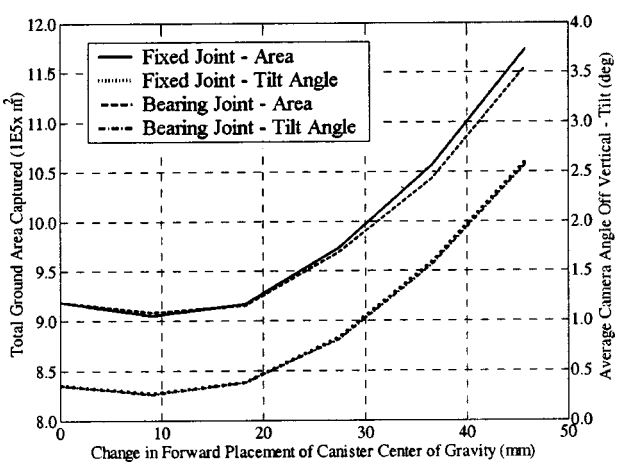

Fig. 18 Total ground area and average camera angle off vertical versus change in forward placement of the canister center of gravity

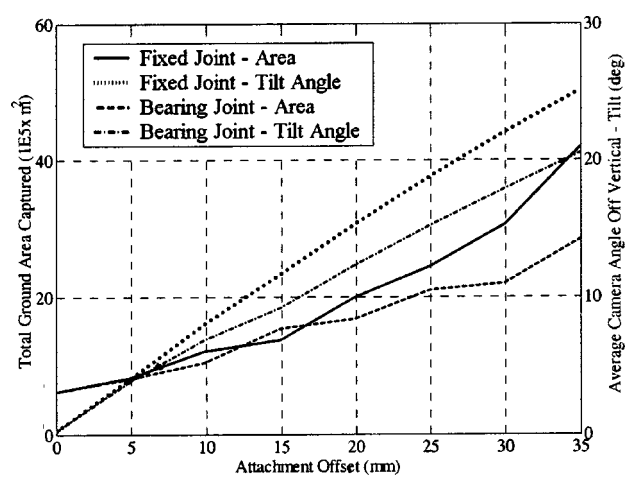

Fig. 20 Total ground area and average camera angle off vertical versus attachment offset

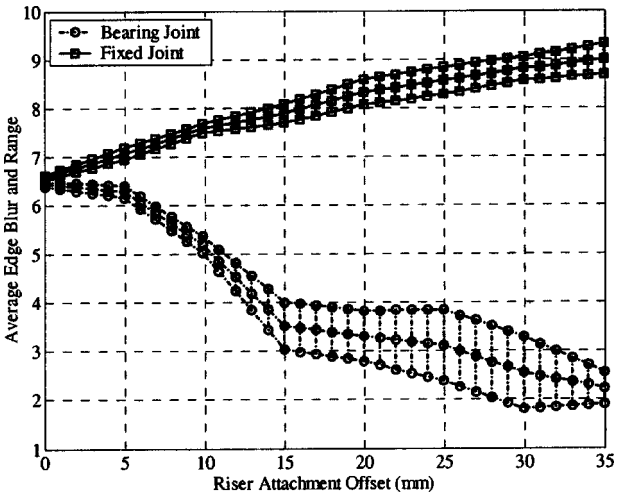

Fig. 21 Average edge pixel blur and range of pixel blur per canister oscillation versus attachment offset

length also induces increased coning of the canister. Another method that is effective in increasing coning, yet subtler is moving the center of gravity of the canister forward. These conclusions provide valuable criteria for designers of munition launched systems and parachute borne imaging systems. The data obtained from these analyses allow designers to evaluate the performance of these systems based on the governing parameters of the coupled systems without the expense of physical testing.

Nomenclature

x, y, z = Position components of the center of mass of the respective body expressed in the inertial reference frame
ϕ, θ, ψ = Euler roll, pitch, and yaw angles of the respective body
u, v, w = Translational velocity components of the center of mass of the respective body expressed in the body reference frame
p, q, r = Angular velocity components of the respective body expressed in the body reference frame
X, Y, Z = External forces on the respective body expressed in the body reference frame
m = Mass of the respective body
I = Inertia matrix of the respective body
L, M, N = External moments on the respective body expressed in the body reference frame
W = Weight of the respective body
ρ = Density of air for the respective body
V = Velocity magnitude of the respective body
A = Reference area of the respective body
D = Reference diameter of the respective body
C_{Z0} = Drag force alpha-to-the-zero coefficient
C_{Z2} = Drag force alpha-squared coefficient
C_{NA} = Projectile normal force coefficient
α = Longitudinal angle of attack of the respective body
β = Lateral angle of attack of the respective body
C_{LDD} = Roll moment due to fin cant coefficient
C_{LP} = Roll damping moment coefficient
C_{MQ} = Pitch damping moment coefficient
C_T = Tangential force coefficient
C_N = Normal force coefficient
P_S = Sixth order polynomial as a function of time used to describe the expulsion charge
n_X, n_Y, n_Z = Directional unit vector components
C_{DD} = Roll generation coefficient
r_X, r_Y, r_Z = Position vector components from the center of mass of the canister to the image plane points
P_L = Pixel size
P_X = Pixel scale
P_B = Pixel blur, number of pixels traversed in one exposure
x_c, y_c, z_c = Translational position components of the canister center of gravity expressed in the inertial reference frame
x_f, y_f, z_f = Translational position components of the imager focal point expressed in the inertial reference frame
x_i, y_i, z_i = Translational position components of the center and corner points of the image plane expressed in the inertial reference frame
x_g, y_g, z_g = Translational position components of the projected image points in the ground plane expressed in the inertial reference frame
V_g = Velocity of the projected image points in the ground plane, $\sqrt{\dot{x}_g^2+\dot{y}_g^2}$
t_{ss} = Effective shutter speed of imager

Subscripts

A = Represents forces due to aerodynamics
W = Represents forces due to weight
S = Represents forces due to separation
R = Represents forces due to the riser connection

References

[1] White, F. M., and Wolf, D. F., 1966, "A Theory of Three-Dimensional Parachute Dynamic Stability," AIAA Aerodynamic Deceleration Systems Conference, Houston, TX, September 7–9.
[2] Wolf, D., 1970, "Dynamic Stability of a Nonrigid Parachute and Payload System," AIAA 8th Aerospace Sciences Meeting, New York, January 19–21.
[3] Shpund, Z., and Levin, D., 1994, "Static and Dynamic Coefficients of a Cross-Type Parachute," J. Aircr., **31**, pp. 132–137.
[4] Doherr, K. F., and Schiling, H., 1991, "9DOF-Simulation of Rotating Parachute Systems," AIAA 12th Aerodynamic Decelerator and Ballon Tech. Conf.
[5] Neustadt, M., Ericksen, R. E., Guiteras, J. J., and Larrivee, J. A., 1966, "A Parachute Recovery System Dynamic Analysis," AIAA Paper No. 66–25, 3rd Aerospace Science Meeting, New York.
[6] Shpund, Z., and Levin, D., 1997, "Forebody Influence on Rotating Parachute Aerodynamic Properties," J. Aircr., **34**, pp. 181–186.
[7] Hutchins, R. G., and Sworder, D. D., 1991, "Image Fusion Algorithms for Tracking Maneuvering Targets," J. Guid. Control Dyn., **15**, pp. 175–184.
[8] Rastogi, A. K., Chatterji, B. N., and Ray, A. K., 1997, "Design of a Real-Time Tracking System for Fast-Moving Objects," IETE J. Res., **43**, pp. 359–369.
[9] Gilbert, A. J., Giles, M. K., Flachs, G. M., Rogers, R. B., and Yee, H. U., 1980, "A Real-Time Video Tracking System," IEEE Trans. Pattern Anal. Mach. Intell., **PAMI-2**, pp. 47–56.
[10] Smith, S. M., and Brady, J. M., 1994, "A Scene Segmenter: Visual Tracking of Moving Vehicles," Eng. Applic. Artif. Intell., **7**, pp. 191–204.
[11] Chen, L., and Chang, S., 1992, "A Video Tracking System With Adaptive Predictors," Pattern Recogn., **25**, pp. 1171–1180.
[12] Pei, S., and Liou, L., 1998, "Vehicle-Type Motion Estimation by the Fusion of Image Point and Line Features," Pattern Recogn., **31**, pp. 333–344.
[13] Mohanty, N. C., 1981, "Computer Tracking of Moving Point Targets in Space," IEEE Trans. Pattern Anal. Mach. Intell., **PAMI-3**, pp. 606–611.
[14] Lee, H., Huang, L., and Chen, Z., 1990, "Multi-Frame Ship Detection and Tracking in an Infrared Image Sequence," Pattern Recogn., **23**, pp. 785–798.
[15] Kundur, S., and Ravin, D., 2000, "Active Vision-Based Control Schemes for Autonomous Navigation Tasks," Pattern Recogn., **33**, pp. 295–308.
[16] Kerr, D., Bouazza-Marouf, K., and West, T. C., 1999, "An Inexpensive Pointing and Tracking System Using TV Cameras and an Optical Fibre Beacon, *Mechatronics*," **9**, pp. 919–927.
[17] Azarbayejani, A. J., and Alexander, H. L., 1991, "Vision Navigator for Free-Flying Robots," Proc. SPIE, **1612**, pp. 257–265.
[18] Sandwich, S., 1998, "Real-Time Videogrammetry Uncertainty Computation and Test Results," Proc. SPIE, **3520**, pp. 111–122.
[19] Schalkoff, R. J., 1982, "A Model and Tracking Algorithm for a Class of Video Targets," IEEE Trans. Pattern Anal. Mach. Intell., **PAMI-4**, pp. 2–10.
[20] Best, L., and Magee, M., 1998, "Autonomous Construction of Three-Dimensional Models From Range Data," Pattern Recogn., **31**, pp. 128–136.
[21] Mitchell, E. N., 1984, *Photographic Science*, John Wiley & Sons, Inc.
[22] Moffet, F. H., and Mikhail, Edward M., 1980, *Photogrammetry*, Harper & Row.
[23] Kasser, M., and Egels, Y., 2002, *Digital Photogrammetry*, Taylor & Francis.

[24] Jensen, J. R., 1996, *Introductory Digital Image Processing A Remote Sensing Perspective*, Prentice–Hall, Inc.
[25] Avery, T. E., and Berlin, G. L., 1985, *Fundamentals of Remote Sensing and Airphoto Interpretation*, Prentice–Hall, Inc.
[26] Von Mises, R., 1959, *Theory of Flight*, Dover Publications Inc.
[27] PRODAS—Projectile Design and Analysis, Arrow Tech Associates, Inc., 1233 Shelburne Road, Suite D-8, Pierson House, South Burlington, VT 05403, 2002.
[28] Wolfe, W. P., and Peterson, C. W., ''Modeling of Parachute Suspension Line Wrap,'' AIAA with permission, Sandia National Laboratories, 2001, AIAA-2001-2025.
[29] ''MIT Digital Orthophoto Browser,'' *Massachusetts Geographical Information Systems: Massachusetts Executive Office of Environmental Affairs*, Planning_Support Systems Group, M.I.T. Department of Urban Studies and Planning, 5 February, 1998, http://ortho.mit.edu/nsdi/index.html.